Research paper

Noble metal-free near-infrared-driven photocatalyst for hydrogen production based on 2D hybrid of black Phosphorus/WS$_2$

Mingshan Zhu[a], Chunyang Zhai[b], Mamoru Fujitsuka[a], Tetsuro Majima[a,*]

[a] *The Institute of Scientific and Industrial Research (SANKEN), Osaka University, Mihogaoka 8-1, Ibaraki, Osaka 567-0047, Japan*
[b] *School of Materials Science and Chemical Engineering, Ningbo University, Ningbo 315211, PR China*

A B S T R A C T

Efficient production of H$_2$ from water using solar energy holds tremendous promise for clean energy. The optimal photocatalysts require earth abundant elements for the cost-effective as well as harvesting broad spectrum of solar light, particularly in the near-infrared (NIR) region. Therefore, pathways leading to NIR-driven H$_2$ production activity on noble metal-free photocatalyst are of high scientific and economic interest. Here we report a binary two dimensional (2D) hybrid of black phosphorus (BP) and WS$_2$ as noble metal-free NIR-driven photocatalyst for H$_2$ production. Under > 780 nm NIR light irradiation, substantive H$_2$ productions were observed. Compare to pure BP and WS$_2$, the solid enhancement (21 and 50 folds) of photocatalytic activity was achieved in the BP/WS$_2$ hybrid. The mechanism has been investigated by photoelectrochemical measurements, electron reductive reaction analyses, and transient absorption spectroscopy. It is indicated that 2D BP/WS$_2$ hybrid has great potential as a noble metal-free NIR-driven photocatalyst for solar energy conversion.

1. Introduction

Hydrogen (H$_2$), as a zero carbon emission fuel, is to be the most clean and a renewable energy source. Since the first discovery of photoelectrochemical water splitting to H$_2$ and O$_2$ by Fujishima and Honda in 1972 [1], H$_2$ production from photocatalytic water splitting has been one of the hottest research topics in the past decades [2–6]. From economic reasons, the highly effective photocatalysts made by earth-abundant elements are required [5–9]. Phosphorus (P) is one of the most abundant elements in the earth crust (*ca.* 0.1% of the earth crust) [10]. The elemental phosphorus generally has several allotropes, such as white, red, and black phosphorus. Recently, Yu's group firstly discovered the probability of using elemental red phosphorus (RP) as a semiconductor for photocatalytic water splitting to H$_2$ [11]. Furthermore, by using small-sized fibrous phosphorus, they obtained the highest records in the family of elemental photocatalysts for H$_2$ production under visible-light irradiation [12]. Although a breakthrough on above elemental photocatalyst was obtained, still two key points need to be considered. Firstly, in order to utilize the maximization of solar energy, studies aimed at utilizing near-infrared (NIR) light, which accounts for approximately 44% in our incoming solar spectrum, are rather limited [13,14]. Secondly, noble metal such as platinum (Pt) must be used as extra cocatalysts, whereas the high-cost and limited-reserves of Pt demand to explore alternative noble metal-free catalysts

with low-cost [3,4].

Currently, ultrathin two dimensional (2D) materials grab a big triumph in optics, electronics, catalysis, and so on [15]. As a new 2D member, ultrathin black phosphorus (BP) has received more and more attentions since the first report on field-effect transistors in 2014 [10,16–19]. Because of the direct bandgap of BP can be adjusted from ~0.3 eV for bulk BP to ~2.1 eV for BP monolayer, 2D BP is chosen to be a promising visible and NIR-activated functional material in the application of optical and photocatalysis [20–29]. However, the rapid recombination of photogenerated electron-hole pairs in pure BP retards the reaction of H$_2$ production. 2D-layered transition metal disulfides (TMDs) nanosheets have been regarded as promising candidates to replace Pt for H$_2$ production in recent years [30]. Among TMDs, tungsten disulfide (WS$_2$) exhibits a promising activity owing to its intrinsic electronic properties, which allow it to be an efficient co-catalyst over photo-harvesting semiconductors in H$_2$ production [30–32].

Herein, by using BP and WS$_2$, for the first time, we develop a noble metal-free photocatalytic H$_2$ production system that responds to a wide spectrum of solar light, particularly in the NIR region. Compared to trace H$_2$ production by the single component, the optimum H$_2$ production rates of BP/WS$_2$ hybrid reached to 2.49 and 1.55 μmol under > 780 nm and 808 nm NIR laser light irradiation, respectively. 2D WS$_2$ plays a crucial role in the improvement of photocatalytic performance by trapping the photogenerated electrons from excited BP,

causing water reduction to H_2. To get clear proofs of the photocatalytic H_2 production mechanism, the photoelectrochemical (PEC) properties, electron reductive reaction (ERR), and transient absorption spectroscopy (TAS) were investigated. The present results show 2D BP/WS_2 as a noble-metal-alternative NIR activated photocatalyst for H_2 production, contributing to a new paradigm for designing cost-effective artificial photosynthesis system in energy conversion.

2. Results and discussion

Both WS_2 and BP nanoflakes were obtained by a *N*-methyl-2-pyrrolidone (NMP) solvent exfoliation method. The fine morphologies of as-prepared WS_2 and BP nanoflakes were studied by means of transmission electron microscopy (TEM) and atomic force microscopy (AFM). Firstly, 2D flake-like structure of WS_2 and BP nanoflakes can be observed in TEM images (Figs. S1a and b). The sizes of as-prepared WS_2 and BP nanoflakes are ranged from 50 to 100 nm and 200 nm–1 μm, respectively. The crystallinity of the as-prepared samples was studied by high-resolution TEM (HRTEM). Clear lattice fringes with d-spacing of 0.27 nm and 0.22 nm were observed to be assigned to the (100) and (002) planes for WS_2 and BP nanoflakes, respectively (Fig. S1c and d) [24,33]. Furthermore, as shown in Fig. S2a, the thickness of as-exfoliated BP nanoflakes ranging from 3.6 to 4.7 nm was observed to be close to that of the 5–8 phosphorus atomic layers according to the monolayer thickness of 0.5–0.7 nm [34]. For as-exfoliated WS_2, the thickness ranging from 6.8 to 15.3 nm was detected, suggesting a few layers of atomic WS_2 (Fig. S2b).

Due to 2D structures of both WS_2 and BP, the small-sized WS_2 nanoflakes are easily assembled on the surface of BP nanoflakes. Fig. 1 shows the low-resolution TEM (LRTEM), TEM, and HRTEM images of as-prepared BP/WS_2 hybrids. The small irregular sheet-like WS_2 nanoflakes were found on the surface of BP nanoflakes, as shown in Fig. 1a and b. To show the components in BP/WS_2 hybrid, HRTEM images from three different areas (dotted circle) were chosen (Fig. 1c–f) from Fig. 1b. Firstly, in the area of Fig. 1d′, only BP's lattice fringes with d-spacing of 0.22 nm (assigned to (002) plane) were observed, suggesting that the support sheet is BP nanoflakes. Secondly, from area of Fig. 1e′ and f′, clear WS_2's lattice fringes with d-spacing of 0.27 nm (assigned to (100) plane) and 0.62 nm (assigned to (002) plane) were detected. Moreover, some lattice fringes corresponding to BP were also observed in the area of Fig. 1f′. These results indicate the sheets on the BP surface are WS_2 nanoflakes.

To analyze the compositions of BP and WS_2 in BP/WS_2 hybrid, the high-angle annular dark field scanning transmission electron microscopy (HAADF-STEM) images and corresponding energy-dispersive X-ray spectroscopy (EDX) elemental mappings, and EDX spectra of BP/

WS_2 were measured, as shown in Figs. 2 and S3, S4 . From Fig. 2a and b, we can easily find different layers of two components. The elemental mappings of P, W, and S elements give more clear images for the components in BP/WS_2 hybrid, indicating a successful hybridization of BP and WS_2. A EDX spectrum (Fig. 2f) shows existence of all three elements of P, W, and S in above selected HAADF-STEM area, confirming the formation of BP/WS_2 nanocomposites. To further confirm the contents of BP and WS_2, the HAADF-STEM, corresponding EDX elemental mappings, and a EDX spectrum for an enlarge area in Fig. 2a were studied. As shown in Figs. S3 and S4, the contents of BP and WS_2 in BP/WS_2 hybrid are much easier observed.

To investigate the chemical configurations and interaction between WS_2 and BP in BP/WS_2 hybrid, the XPS spectra of W 4f, S 2p, and P 2p of samples were measured as shown in Fig. 3a–c. In the spectra of WS_2, two characteristic peaks corresponding to the binding energies for W $4f_{7/2}$ and W $4f_{5/2}$, and S $2p_{3/2}$ and S $2p_{1/2}$ are detected at *ca.* 32.9 and 35.1 eV, and 162.6 and 163.8 eV, respectively [14]. However, when WS_2 was hybridized with BP, all characteristic peaks of W 4f and S 2p were shifted to lower binding energies in the XPS spectra (32.7 and 34.9 eV, and 162.3 and 163.5 eV, respectively). For pure BP, three bands at *ca.* 129.7, 130.5, and 134.1 eV corresponding to P $2p_{3/2}$, P $2p_{1/2}$, and oxidized phosphorus (P_xO_y), respectively, were detected [27,34]. Oppositely, for BP/WS_2, these characteristic peaks were shifted to higher binding energies (129.9, 130.7, and 134.4 eV, respectively). Generally, in the composite, the binding energy shift means a strong interaction between two components. Moreover, the higher and lower binding energy shifts for BP and WS_2 in BP/WS_2 hybrid are ascribed to the decrease and increase of the electron density, suggesting that BP and WS_2 are acted as an electron donor and acceptor in the BP/WS_2 hybrid, respectively [35,36].

To study the optical properties of the as-prepared samples, the UV–vis spectra were measured, as shown in Fig. 3d. Pure BP nanoflakes display a very broad absorption from UV to NIR region, whereas pure WS_2 nanoflakes show main absorption in the visible region. The peaks at around 527 and 633 nm are assigned to excitons from two spin-orbit split transitions at the *K* point of the Brillouin zone [37,38]. When WS_2 nanoflakes are hybridized with BP, the spectral shape is close to the overlap of BP and WS_2. The weak absorption of WS_2 in BP/WS_2 hybrid is due to the low weight ratio (10 wt%) of WS_2 in BP/WS_2. Furthermore, the typical peak of WS_2 in BP/WS_2 shifts to 639 nm. This phenomenon further indicates an interaction of between and WS_2 in BP/WS_2 hybrid.

Based on above optical properties, BP/WS_2 has distinctly absorption in the NIR region, indicating a potential advantage as a NIR light-induced photocatalyst. Accordingly, the photocatalytic H_2 production was evaluated over a BP/WS_2 hybrid in the presence of
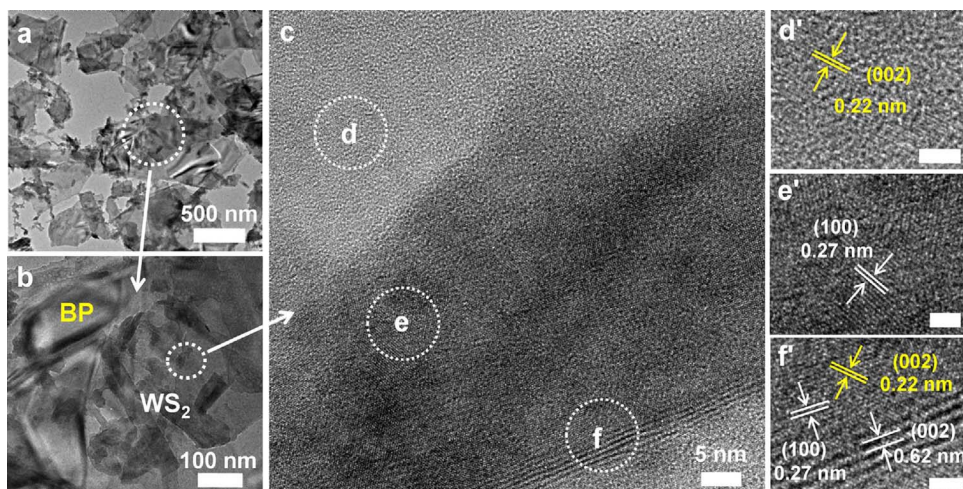

Fig. 1. LRTEM (a), TEM (b), and HRTEM (c-f,d′-f′) images of BP/WS_2 hybrid. The scale bar in Fig. 1d′–f′ is 2 nm.
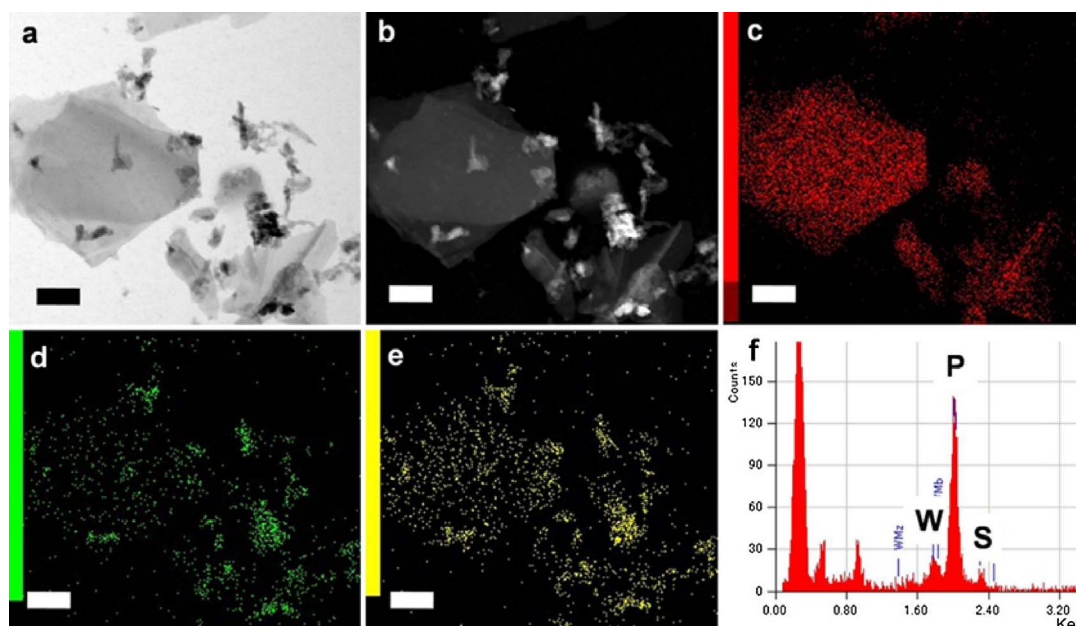
Fig. 2. HAADF-STEM image of dark-field (a and b) and corresponding EDX elemental mapping of P (c), W (d), and S (e) of BP/WS$_2$ hybrid. The scale bar in above panels is 200 nm. EDX spectrum of BP/WS$_2$ hybrid (f). The signals from 0 to 1 eV are C, O, and Cu, respectively, which come from the substrate of Cu grid coated with carbon.
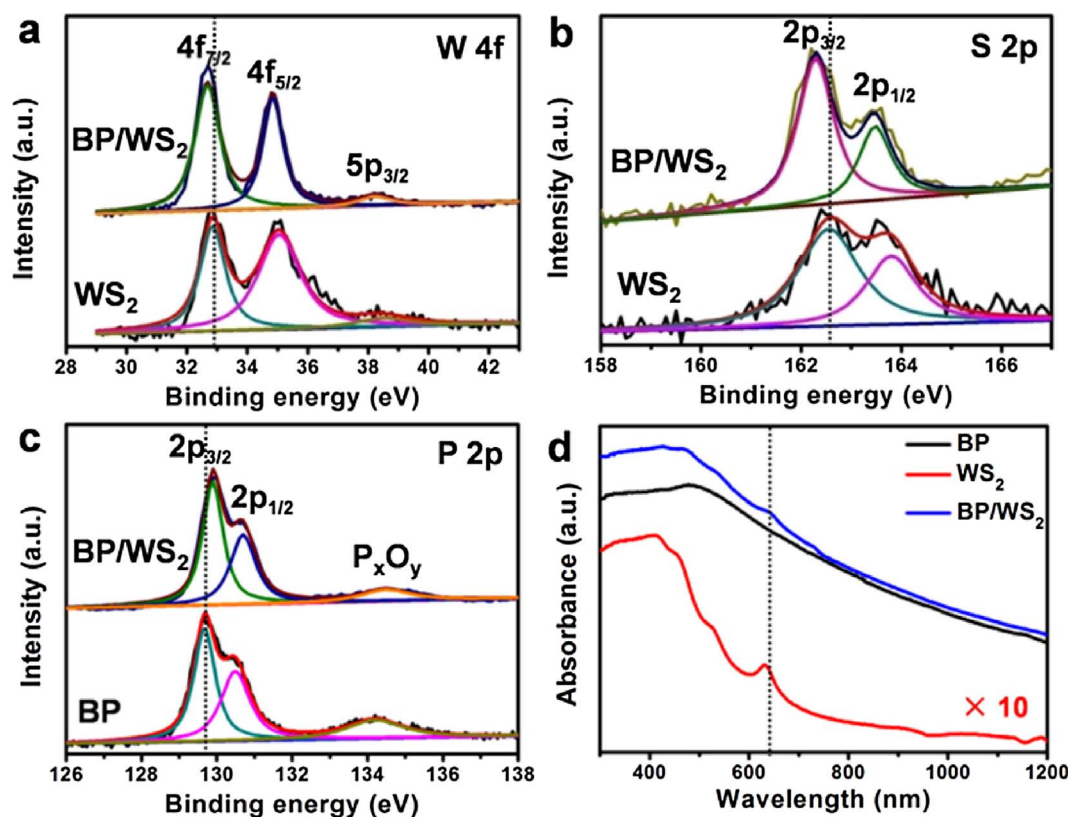

Fig. 3. XPS spectra of W 4f (a), S 2p (b), and P 2p (c), and UV–vis spectra of BP, WS$_2$, and BP/WS$_2$ hybrid (d).

ethylenediaminetetraacetic acid (EDTA) as a sacrificial agent. A Xenon lamp (output wavelength: 350–1800 nm) with a 780 nm long-pass filter in front of the reactor was used. As shown in Fig. 4a, substantial H$_2$ (2.49 μmol) was detected under 3 h NIR light irradiation. However, only trace H$_2$ was detected with pure BP (0.12 μmol) and WS$_2$ (0.05 μmol) nanoflakes under the same conditions. The limited activities of pure BP and WS$_2$ are attributed to their intrinsic fast recombination of photoinduced charge carriers. Compare to pure BP and

WS$_2$, the solid enhancement (21 and 50 folds) of photocatalytic activity in BP/WS$_2$ suggests that WS$_2$ is served as an efficient cocatalyst for H$_2$ production. The apparent quantum efficiencies (AQEs) is as high as approximately and 2.06% at 780 ± 5 nm. The turnover numbers (TONs) of above experiments for BP and WS$_2$ are 0.39 and 3.1, respectively. To further explore the NIR activated photocatalytic performance of BP/WS$_2$, a 808 nm NIR laser was used as the light source. *ca.* 1.55 μmol H$_2$ was produced under 808 nm laser light irradiation for 3 h.
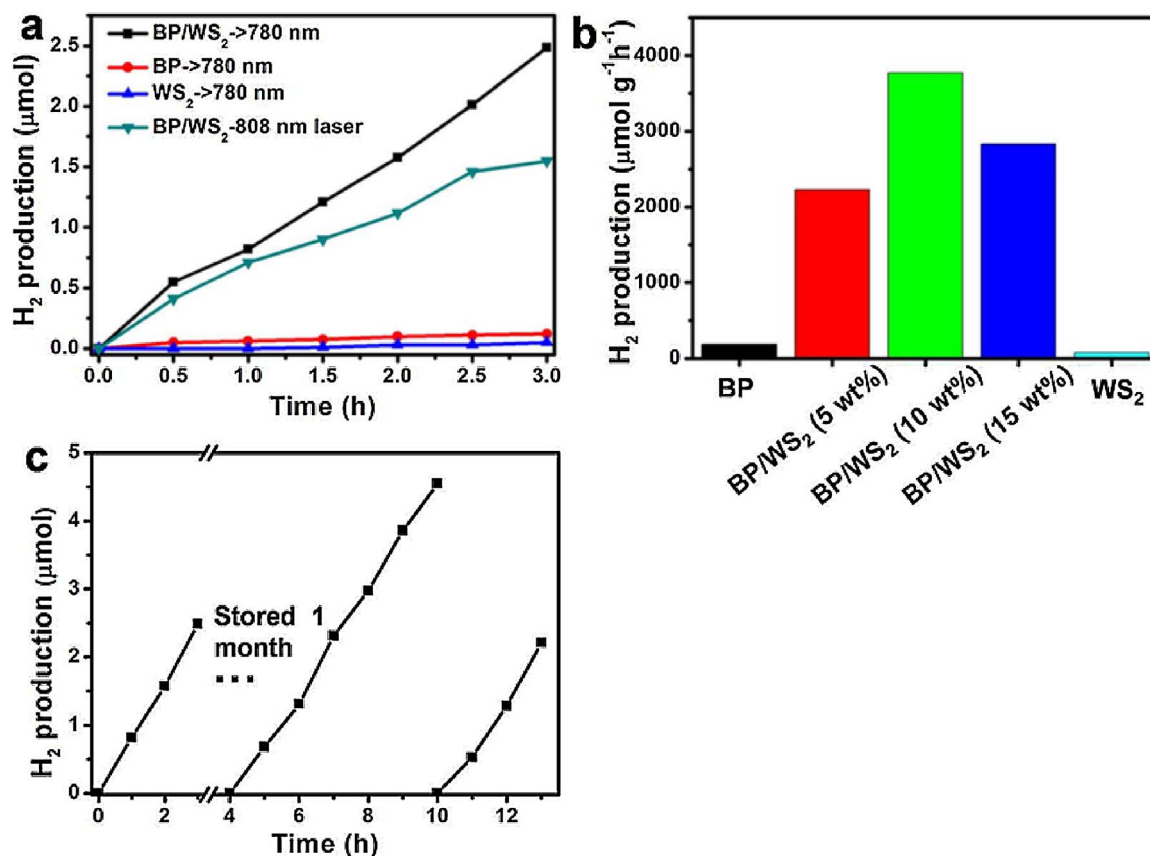
Fig. 4. Photocatalytic H_2 production from water on catalysts under > 780 nm and 808-nm laser light irradiation (a). Effect of weight ratio of WS_2 on BP/WS_2 for photocatalytic H_2 production rate under > 780 nm irradiation (b). Cycle stability test on BP/WS_2 photocatalytic H_2 production under > 780 nm irradiation (c).

These results solidly indicate that BP/WS_2 works as a NIR-activated photocatalyst for the splitting water to H_2. We summarized recent reports of the representative NIR-activated photocatalysts (Table S1). Compared to other systems, it can be clearly to see that the BP/WS_2 displays superior catalytic activity in the NIR region.

Moreover, the influence of the weight ratio of WS_2 in BP/WS_2 hybrid on H_2 production was investigated. As shown in Fig. 4**b**, the optimal weight ratio of WS_2 in BP/WS_2 hybrid for photocatalytic H_2 production is 10 wt%. Further increase in the ration leads to lower activity, probably owing to the decrease of photon absorption by WS_2 [39]. The photocatalytic durability of BP/WS_2 for H_2 production was investigated by cyclic experiments. After the first time reaction, the catalysts were stored for one month. Fig. 4**c** shows continuous H_2 production with no noticeable decrease in the subsequent runs. Furthermore, the TEM, XPS, and UV–vis spectra of BP/WS_2 after photocatalytic reaction showed no obvious change (Figs. S5–S7). These results indicate that the as-prepared BP/WS_2 hybrid kept stable during photocatalytic H_2 production.

The photocatalytic activities of H_2 production under different wavelength of monochromatic light were investigated. Fig. S8 shows that the BP/WS_2 still has activity under 1000 nm excitation. However, under excitation at 1200 nm, only trace amount of H_2 was detected. The negligible activity at longer wavelength is because of relative poor photon absorption and photon energy-dependent photoreaction with lower hot electron injection yields at longer wavelength. Moreover, the photocatalytic H_2 evolution activity of BP/WS_2 was measured under simulated solar ($\sim$100 mW cm^{-2}) irradiation to evaluate solar energy conversion. Fig. S9 shows that approximately 9.61 μmol H_2 was obtained, suggesting a high-performance of photocatalytic H_2 production of BP/WS_2 under solar light irradiation.

Above results suggest an effective charge separation in BP/WS_2 hybrid contributing to the enhancement of photocatalytic performance.

To demonstrate such interfacial charge transport between BP and WS_2 under NIR light irradiation, photocurrent responses, current density-potential ($J-V$), and electrochemical impedance spectroscopy (EIS) were studied (Fig. 5). As shown in Fig. 5A, when BP, WS_2, and BP/WS_2 modified electrodes were used as a working electrode, response photocurrents with repeatable on/off cycles upon NIR light irradiation were observed. The average photocurrent for BP/WS_2 is approximately 0.02 mA cm^{-2} to be 3.3 and 5.0 times larger than those of pure BP (0.006 mA cm^{-2}) and WS_2 (0.004 mA cm^{-2}), respectively. This enhanced photoresponse of BP/WS_2 displays higher efficiency of interfacial charge transport in BP/WS_2 hybrid. On the other hand, the $J-V$ curves of above electrodes were shown in Fig. 5B . Firstly, in dark condition, the BP/WS_2 (1.24 mA cm^{-2}) showed the highest current density compared to pure BP (0.89 mA cm^{-2}) and WS_2 (1.11 mA cm^{-2}). Secondly, when above electrodes were irradiated with NIR light, the current densities of all electrodes were improved greatly, suggesting an efficient photo-enhanced phenomenon. The electrons generated by NIR excitation result in higher photocurrent densities. Same to dark condition, compared with BP and WS_2, BP/WS_2 hybrid showed the highest current density as large as 2.29 mA cm^{-2}. These results indicate that BP/WS_2 hybrid not only shows higher charge separation efficiency compared to pure BP and WS_2 but also displays an effective NIR photo-response activity.

In addition, to verify the excellent electron mobility and internal resistance of BP/WS_2, EIS spectra of above electrodes under dark and NIR light irradiation were measured. In the EIS analysis, the diameter of semicircle arc is used to evaluate the interfacial electron transport. Smaller semicircle arc generally means faster interfacial electron transfer [40]. Without NIR irradiation, the diameter of the semicircle arc for BP/WS_2 hybrid displays much smaller than that of a pure BP or WS_2 modified electrode (Fig. 5C), indicating an efficient interfacial electron mobility in BP/WS_2 hybrid. When these electrodes were
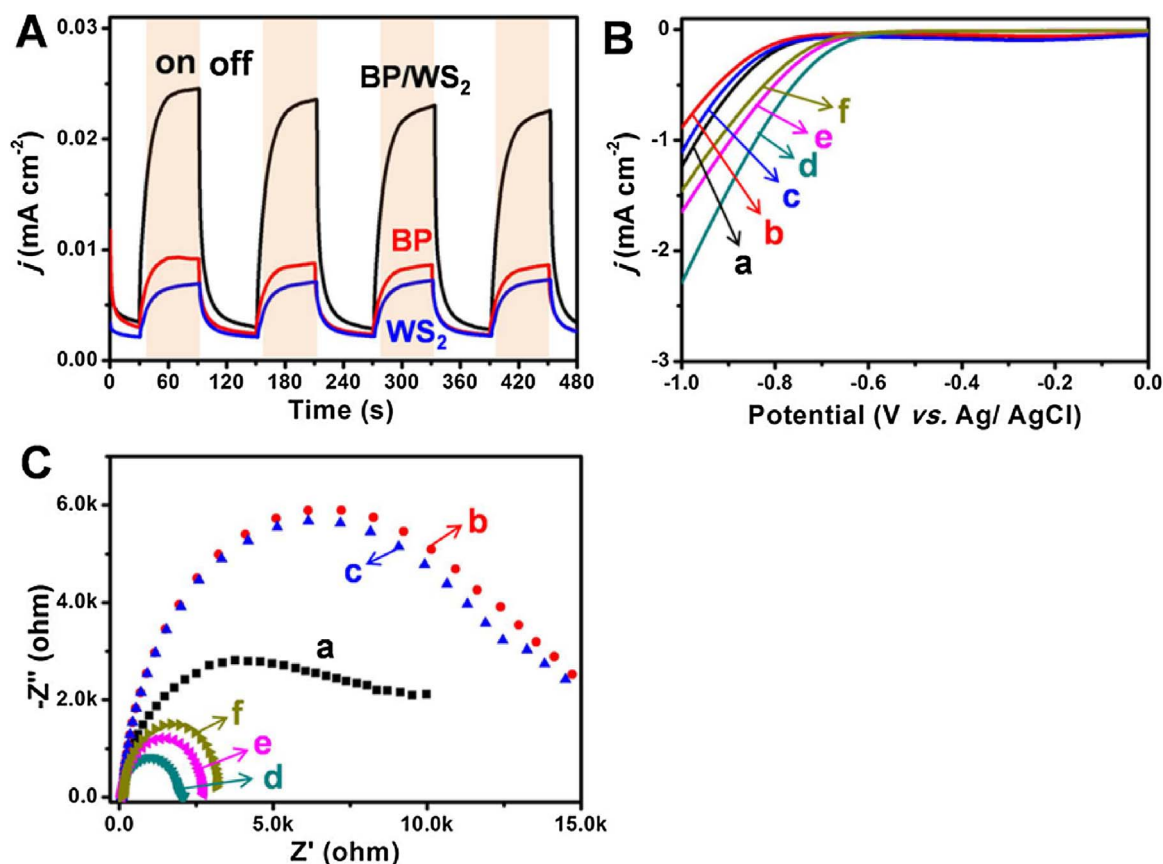
Fig. 5. (A) Photocurrent responses of BP, WS_2, and BP/WS_2 hybrid under > 780 nm irradiation. (B) *J-V* curves and (C) EIS spectra of BP/WS_2 (a and d), BP (b and e), and WS_2 (c and f) in 0.1 M NaOH ethanol solution under dark (a, b, and c) and > 780 nm irradiation (d, e, and f).

irradiated with NIR light, diameters of all semicircle arcs decreased, and BP/WS_2 showed the smallest diameter. Corresponding equivalent circuit was used to fit the EIS data (Fig. S10) and the parameters of R_{ct} were summarized in **Table S2**. BP/WS_2 showed the smallest resistance under NIR light illumination, indicating an effective interfacial charge transport upon the NIR- photo-irradiation.

Although above photoelectrochemical properties reveal information on efficient charge transfer in BP/WS_2 hybrid, the dynamics of electrons in photocatalysts are curial to gain an understanding of the photo-catalytic reaction. Generally, TAS is a powerful tool to analyze the dynamic of photoexcited state [41–44]. Therefore, the TAS of our samples was investigated under 780 nm excitation. Usually, transient absorption bands in the NIR region represent the trapped e^- in the TAS [45]. As shown in Fig. 6, the time profiles of absorption probed at 950 nm of BP show a lifetime of 241 ps. However, when BP/WS_2 was excited, the lifetime of electron was 90.4 ps. Considering the negligible signal of transient absorption from pure WS_2, such observed TAS is attributable to electron in BP. Compared to pure BP, the shorten life-time of BP/WS_2 is explained by the interfacial electron transfer from excited BP to adjacent WS_2. Similar phenomena were observed by other's reports [46–48].

Based on above analyses, the mechanism for photocatalytic H_2 production by BP/WS_2 hybrid under NIR illumination is proposed, as shown in Scheme 1. Firstly, based on UV–vis diffuse reflectance spectra modified by Kubelka–Munk function and Mott–Schottky plots (Fig. S11), the conduction band (CB) and valence band (VB) of BP were *ca.* −0.18 V and 0.52 V *vs.* NHE (4.32 eV and 5.02 eV *vs.* vacuum level), respectively. Thus, as-prepared BP can be excited under NIR light ex-citation and then generates electrons and holes in the CB and VB, re-spectively. The CB level of BP is suitable for H_2 generation when BP is photoexcited. However, due to rapid charge recombination, pure BP
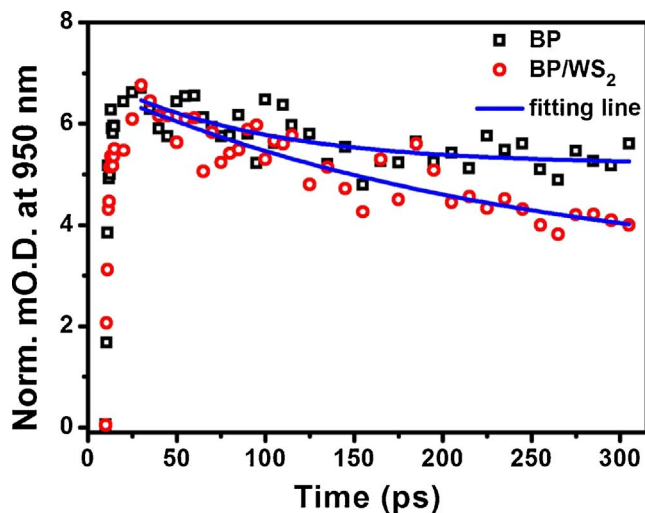

Fig. 6. Transient absorption traces observed at 950 nm for BP and BP/WS_2 under 780 nm excitation.

shows a negligible photocatalytic activity on H_2 generation. However, in BP/WS_2 hybrid, due to the interaction with WS_2, the CB electrons in BP are efficiently injected to WS_2 nanoflakes owing to the lower work function of WS_2 (5.57 eV) [49]. After enough electrons are trapped by WS_2, the reduction of H^+ (water) occurs to generate H_2. Accordingly, the existence of WS_2 offers more opportunities for charge separation promoting the photogenerated electrons to participate in water reduc-tion to H_2. Finally, holes in the VB band of BP are captured rapidly by EDTA as a sacrificial electron donor.

To visually show the effective reductive reaction on BP/WS_2 hybrid,
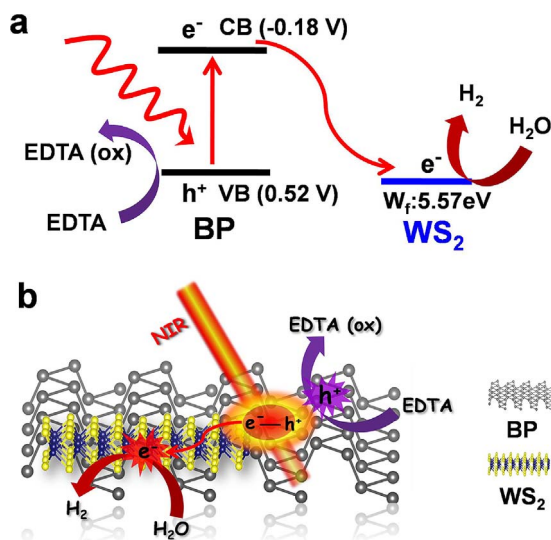
Scheme 1. Proposed schematic diagram for the NIR light activated photocatalytic H$_2$ production of BP/WS$_2$ hybrids in the presence of EDTA.

an electron reductive reaction (ERR) was investigated by using typical reductive probe molecule, resazurin [50]. The reductive reaction scheme for resazurin was shown in Fig. S12. After the system was achieved an equilibrium adsorption state, the photoreaction of resazurin was monitored by measuring the real-time UV–vis absorption and fluorescence emission (the excitation wavelength was 532 nm) under NIR light irradiation (Fig. 7). As shown in Fig. 7a and d, a control experiment of pure resazurin solution under NIR light irradiation was firstly carried out. The UV–vis absorption and fluorescence spectra did not show obvious change after NIR light irradiation for 40 min, suggesting that pure resazurin is stable under NIR light irradiation. However, when BP was used as a photocatalyst, the peak intensity at 602 nm decreased obviously with an increase of light irradiation time (Fig. 7b). This phenomenon suggests that resazurin is transformed to resorufin in the presence of photogenerated electrons. To further clear see this

transformation, the fluorescence emission spectra were shown in Fig. 7e. It is found that the fluorescence emission at 580 nm distinctly increased with light irradiation. After NIR light irradiation for 40 min, the intensity of fluorescence emission around 580 nm increased by 11.0 times. However, when BP/WS$_2$ was used, the efficiency for the transformation of resazurin to highly fluorescent resorufin was greatly improved (Fig. 7c and f). The fluorescence emission around 580 nm increased 36.8-folds compared to original peak. Accordingly, the existence of WS$_2$ plays a crucial role in the improvement of an electron reductive reaction under NIR light irradiation. These results indicate that in BP/WS$_2$ hybrid, much more effective charge separation limits the recombination of the photogenerated electron-hole pairs.

3. Conclusions

In conclusion, a 2D hybrid of BP and WS$_2$ was constructed and for the first time used as a stable noble metal-free photocatalyst for H$_2$ production under NIR light illumination. Compared to trace amount of H$_2$ in pure BP and WS$_2$, solid enhancements of H$_2$ production in BP/WS$_2$ hybrid were reached under > 780 nm and 808 nm NIR laser light irradiation. WS$_2$ not only served as an effective co-catalyst for H$_2$ production but also separated the charge carriers, thereby improved the efficiency of H$_2$ production. The efficient charge separation processes were thoroughly demonstrated by using photoelectrochemical properties, electron reductive reactions, and transient absorption spectroscopy. The present results show advantages of 2D BP/WS$_2$ hybrid to be a noble metal-free NIR-driven photocatalyst and offer a cost-effective way in expanding utilization of solar light.

4. Experimental section

4.1. Materials

Bulk BP and WS$_2$ crystals were purchased from Nanjing XFNANO Materials Tech Co., Ltd. N-methyl-2-pyrrolidone (NMP), ethylenediaminetetraacetic acid (EDTA), resazurin, and all other chemical materials were purchase from Sigma-Aldrich without further purification.
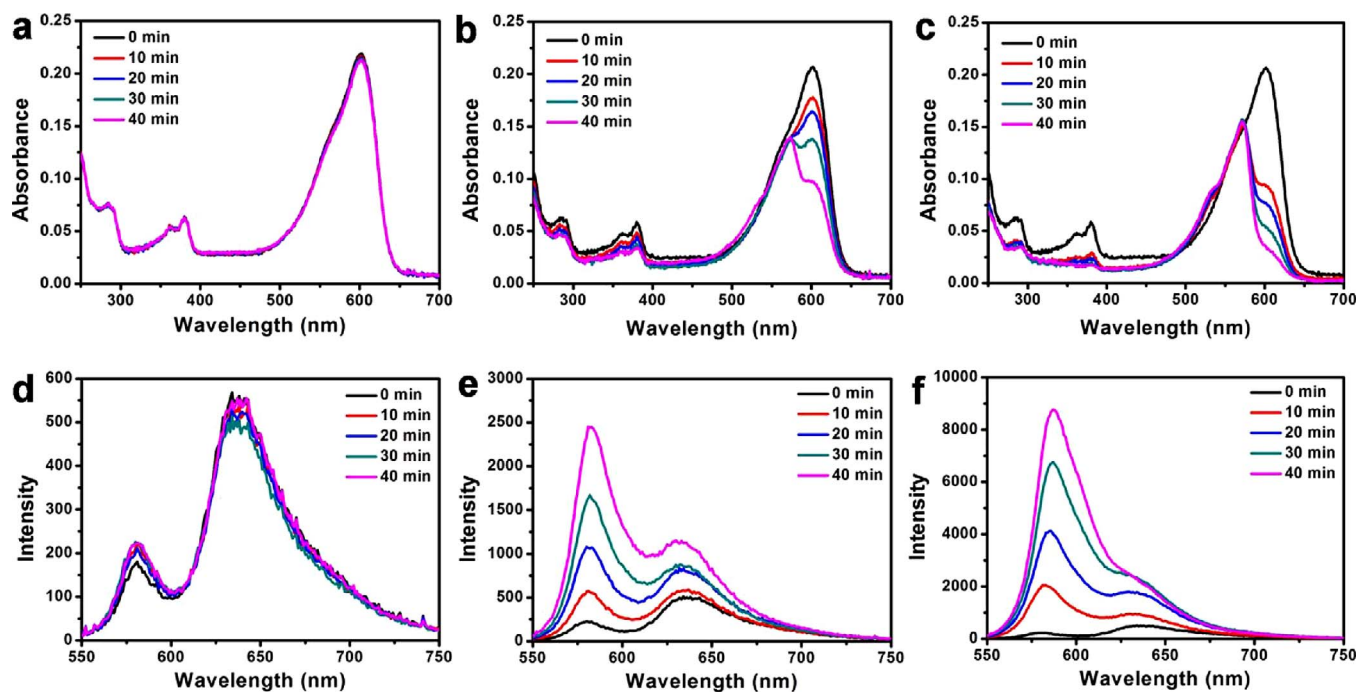
Fig. 7. Real-time UV–vis absorption (a, b, and c) and fluorescence spectra (d, e, and f) of the reductive reaction from resazurin to resorufin for blank (a and d), BP (b and e), and BP/WS$_2$ (c and f) under > 780 nm irradiation.

4.2. Preparation of BP and WS$_2$ nanoflakes

2D BP nanoflakes were synthesized by using a NMP solvent exfoliation [51]. Firstly, 20 mg bulk BP was added into 20 mL NMP. The dispersion was sonicated for 4 h by using a tip sonicator (Misonix XL-2000) at 10 W output power under ice cooling. After that, the dispersion was centrifuged at 2000 rpm for 20 min with two times to remove nonexfoliated bulk BP, resulting in BP nanoflakes NMP dispersions (0.2 mg mL^{-1}). The WS$_2$ NMP dispersions (0.1 mg mL^{-1}) were obtained by similar method expecting that bulk WS$_2$ instead of bulk BP.

4.3. Preparation of BP/WS$_2$ hybrid

BP/WS$_2$ hybrid was prepared as following: 10 mL as-prepared WS$_2$ NMP dispersions were added into 50 mL BP NMP dispersion with sonication for 2 h. The mixtures were kept stirring overnight. Finally, the samples were obtained through high-speed centrifugation and washed with ethanol thoroughly, and then redispersed in 10 mL methanol, resulting in BP/WS$_2$ hybrid. The weight ratio of WS$_2$ to BP was 1:10. The different weight ratio of WS$_2$ and BP was prepared by adding different amount of WS$_2$ nanoflakes.

4.4. Photocatalytic H$_2$ production

0.2 mL BP/WS$_2$ dispersion and 0.2 mL EDTA solution (0.5 M) mixed with 4.6 mL water added into a 35 mL cylinder reactor and sealed with a rubber septum. The system was deaerated by Ar bubbling into the solution for 30 min before the reaction. Before photoreactions, the dispersion was sonicated for 1 min. Afterwards, the system was stirring continuously and irradiating under NIR light by using Xenon lamp (Asahi Spectra, HAL-320W, output wavelength: 350–1800 nm) with a 780 nm cut-off filter. The light intensity is approximately 400 mW cm^{-2}. A 2 W 808 nm portable infrared laser (Highlasers, HK) was used as light source for 808 nm laser NIR light photocatalytic H$_2$ production. The gases produced were analyzed with a gas chromatograph (Shimadzu GC-8A) equipped with an MS-5A column and a thermal conductivity detector (TCD).

The AQE was measured at monochromatic light by using 780 nm band-pass filters. The AQE was calculated as follow:

$$AQE = \frac{N_e}{N_p} \times 100\% = \frac{2 \times n_{H_2} \times N_A \times h \times c}{S \times P \times t \times \lambda} \times 100\%$$

where, N_p is the total incident photons, N_e is the total reactive electrons, n_{H2} is the amount of H$_2$ molecules, N_A is Avogadro constant, h is the Planck constant, c is the speed of light, S is the irradiation area, P is the intensity of irradiation light, t is the photoreaction time and λ is the wavelength of the monochromatic light. For AQE experiment, 5 times of BP/WS$_2$ (i.e., 1.1 mg) were used.

The details of the photoelectrochemical properties, transient absorption (TA), electron reductive reaction (ERR) measurements, and characterizations were summarized in Supporting information.

Acknowledgment

Appendix A. Supplementary data

Supplementary data associated with this article can be found, in the online version, at http://dx.doi.org/10.1016/j.apcatb.2017.09.063.

References

[1] A. Fujishima, K. Honda, Nature 238 (1972) 37–38.
[2] A.A. Ismail, D.W. Bahnemann, Sol. Energy Mat. Sol. C 128 (2014) 85–101.
[3] J.R. Ran, J. Zhang, J.G. Yu, M. Jaroniec, S.Z. Qiao, Chem. Soc. Rev. 43 (2014) 7787–7812.
[4] X.X. Zou, Y. Zhang, Chem. Soc. Rev. 44 (2015) 5148–5180.
[5] C.M. Li, Y. Xu, W.G. Tu, G. Chen, R. Xu, Green Chem. 19 (2017) 882–889.
[6] G.G. Zhang, Z.A. Lan, X.C. Wang, Angew. Chem. Int. Ed. 55 (2016) 15712–15727.
[7] X.C. Wang, K. Maeda, A. Thomas, K. Takanabe, G. Xin, J.M. Carlsson, K. Domen, M. Antonietti, Nat. Mater. 8 (2009) 76–80.
[8] Z.F. Hu, Z.R. Shen, J.G. Yu, Green Chem. 19 (2017) 588–613.
[9] S.A. Ansari, Z. Khan, M.O. Ansari, M.H. Cho, RSC Adv. 6 (2016) 44616–44629.
[10] H. Liu, Y.C. Du, Y.X. Deng, P.D. Ye, Chem. Soc. Rev. 44 (2015) 2732–2743.
[11] F. Wang, W.K.H. Ng, J.C. Yu, H.J. Zhu, C. Li, C.H. Zhang, Z.F. Liu, Q. Li, Appl. Catal. B: Environ. 111–112 (2012) 409–414.
[12] Z.F. Hu, L.Y. Yuan, Z.F. Liu, Z.R. Shen, J.C. Yu, Angew. Chem. Int. Ed. 55 (2016) 9580–9585.
[13] G. Wang, B.B. Huang, X.C. Ma, Z.Y. Wang, X.Y. Qin, X.Y. Zhang, Y. Dai, M.H. Whangbo, Angew. Chem. Int. Ed. 52 (2013) 4810–4813.
[14] Y.H. Sang, Z.H. Zhao, M.W. Zhao, P. Hao, Y.H. Leng, H. Liu, Adv. Mater. 27 (2015) 363–369.
[15] H. Zhang, ACS Nano 9 (2015) 9451–9469.
[16] L.K. Li, Y.J. Yu, G.J. Ye, Q.Q. Ge, X.D. Ou, X.H. Wu, D.L. Feng, X.H. Chen, Y.B. Zhang, Nat. Nanotechnol. 9 (2014) 372–377.
[17] A. Castellanos-Gomez, J. Phys. Chem. Lett. 6 (2015) 4280–4291.
[18] L.Z. Kou, C.F. Chen, S.C. Smith, J. Phys. Chem. Lett. 6 (2015) 2794–2805.
[19] V. Eswaraiah, Q.S. Zeng, Y. Long, Z. Liu, Small 12 (2016) 3480–3502.
[20] M.Z. Rahman, C.W. Kwong, K. Davey, S.Z. Qiao, Energy Environ. Sci. 9 (2016) 709–728.
[21] Z.R. Shen, S.T. Sun, W.J. Wang, J.W. Liu, Z.F. Liu, J.C. Yu, J. Mater. Chem. A 3 (2015) 3285–3288.
[22] H.U. Lee, S.C. Lee, J.H. Won, B.C. Son, S. Choi, Y. Kim, S.Y. Park, H.S. Kim, Y.C. Lee, J. Lee, Sci. Rep. 5 (2015) 8691.
[23] J. Hu, Z.K. Guo, P.E. Mcwilliams, J.E. Darges, D.L. Druffel, A.M. Moran, S.C. Warren, Nano Lett. 16 (2016) 74–79.
[24] H. Wang, X.Z. Yang, W. Shao, S.C. Chen, J.F. Xie, X.D. Zhang, J. Wang, J. Xie, J. Am. Chem. Soc. 137 (2015) 11376–11382.
[25] M. Buscema, D.J. Groenendijk, S.I. Blanter, G.A. Steel, H.S. Zant, A. Castellanos-Gomez, Nano. Lett. 14 (2014) 3347–3352.
[26] S.B. Liu, L.L. Miao, Z.N. Guo, X. Qi, C.J. Zhao, H. Zhang, S.C. Wen, D.Y. Tang, D.Y. Fan, Opt. Express 23 (2015) 11183.
[27] M. Zhu, X. Cai, M. Fujitsuka, J. Zhang, T. Majima, Angew. Chem. Int. Ed. 56 (2017) 2064–2068.
[28] M. Zhu, Y. Osakada, S. Kim, M. Fujitsuka, T. Majima, Appl. Catal. B: Environ. 217 (2017) 285–292.
[29] M. Zhu, S. Kim, L. Mao, M. Fujitsuka, J.Y. Zhang, X. Wang, T. Majima, J. Am. Chem. Soc. 139 (2017) 13234–13242.
[30] K. Chang, X. Hai, J.H. Ye, Adv. Energy Mater. 6 (2016) 1502555.
[31] M.A. Lukowski, A.S. Daniel, C.R. English, F. Meng, A. Forticaux, R.J. Hamers, S. Jin, Energy Environ. Sci. 7 (2014) 2608–2613.
[32] L. Cheng, W. Huang, Q. Gong, C. Liu, Z. Liu, Y. Li, H. Dai, Angew. Chem. Int. Ed. 53 (2014) 7860–7863.
[33] Y.C. Du, X.S. Zhu, L. Si, Y.F. Li, X.S. Zhou, J.C. Bao, J. Phys. Chem. C 119 (2015) 15874–15881.
[34] D. Hanlon, C. Backes, E. Doherty, C.S. Cucinotta, N.C. Berner, C. Boland, K. Lee, A. Harvey, P. Lynch, Z. Gholamvand, S.F. Zhang, K.P. Wang, G. Moynihan, A. Pokle, Q.M. Ramasse, N. McEvoy, W.J. Blau, J. Wang, G. Abellan, F. Hauke, A. Hirsch, S. Sanvito, D.D. O'Regan, G.S. Duesberg, V. Nicolosi, J.N. Coleman, Nat. Commun. 6 (2015) 8563–8573.
[35] Z.Y. Zhang, K.C. Liu, Z.Q. Feng, Y.N. Bao, B. Dong, Sci. Rep. 6 (2016) 19221.
[36] M. Zhu, P. Chen, M. Liu, ACS Nano 5 (2011) 4529–4536.
[37] Y.L. Li, A. Chernikov, X. Zhang, A. Rigosi, H.M. Hill, D.A. Zande, D.A. Chenet, E.M. Shih, J. Hone, T.F. Heinz, Phys. Rev. B 90 (2014) 205422.
[38] T.D. Luccio, C. Borriello, A. Bruno, M.G. Maglione, C. Minarini, G. Nenna, Phys. Status Solidi A 210 (2013) 2278–2283.
[39] X. Zong, J.F. Han, G.J. Ma, H.J. Yan, G.P. Wu, C. Li, J. Phys. Chem. C 115 (2011) 12202–12208.
[40] M. Adachi, M. Sakamoto, J.T. Jiu, Y. Ogata, S.J. Isoda, J. Phys. Chem. B 110 (2006) 13872–13880.
[41] I. Robel, V. Subramanian, M. Kuno, P.V. Kamat, J. Am. Chem. Soc. 128 (2006) 2385–2393.
[42] K. Iwata, T. Takaya, H. Hamaguchi, A. Yamakata, T. Ishibashi, H. Onishi, H. Kuroda, J. Phys. Chem. B 108 (2004) 20233–20239.
[43] M. Maruyama, A. Iwase, H. Kato, A. Kudo, H. Onishi, J. Phys. Chem. C 113 (2009) 13918–13923.
[44] J.J.M. Vequizo, H. Matsunaga, T. Ishiku, S. Kamimura, T. Ohno, A. Yamakata, ACS Catal. 7 (2017) 2644–2651.
[45] T. Tachikawa, P. Zhang, Z.F. Bian, T. Majima, J. Mater. Chem. A 2 (2016) 3381–3388.
[46] P. Zhang, T. Tachikawa, M. Fujitsuka, T. Majima, J. Phys. Chem. Lett. 7 (2016) 1173–1179.
[47] X.G. Li, W.T. Bi, L. Zhang, S. Tao, W.S. Chu, Q. Zhang, Y. Luo, C.Z. Wu, Y. Xie, Adv. Mater. 28 (2016) 2427–2431.
[48] A. Furube, T. Asahi, H. Masuhara, H. Yamashita, M. Anpo, Chem. Phys. Lett. 336 (2001) 424–430.
[49] H. Vovusha, B. Sanyal, RSC Adv. 5 (2015) 67427–67434.
[50] J.B. Sambur, T.Y. Chen, E. Choudhary, G.Q. Chen, E.J. Nissen, E.M. Thomas, N.M. Zou, P. Chen, Nature 530 (2016) 77–80.
[51] Z.N. Guo, H. Zhang, S.B. Lu, Z.T. Wang, S.Y. Tang, J.D. Shao, Z.B. Sun, H.H. Xie, H.Y. Wang, X.F. Yu, P.K. Chu, Adv. Funct. Mater. 25 (2015) 6996–7002.